PCCP

Accepted Manuscript




ROYAL SOCIETY OF CHEMISTRY

www.rsc.org/pccp

Journal Name

ARTICLE TYPE

Cite this: DOI: 10.1039/xxxxxxxxxx

# Cross-plane heat transfer through single-layer carbon structures †

Huaichen Zhang,*[a] Silvia V. Nedea,[a] Camilo C. M. Rindt, [a] and David M. J. Smeulders[a]

Received Date
Accepted Date

DOI: 10.1039/xxxxxxxxxx

www.rsc.org/journalname

Graphene-based nano structures are recently proposed to function as additives to improve the conductivity of thermally sluggish phase change materials (PCMs). Based on existing researches, the improvement is dependent not only on the matrix material, but also on the geometry of the carbon structure. To gain more insight into the nano-scale thermal transport problem, we launch the current pilot research using water as the matrix material, to represent the hydroxyl-group-rich sugar alcohols as PCMs. We have found that the heat conduction across a graphene layer to water is much faster than the heat conduction to the graphene layer itself. Also, the high graphene-water thermal contact resistance fails to acknowledge the fast thermal kinetics of the low frequency phonons. In the investigation of the geometry effect, the cross-plane heat transfer coefficient is found to decrease with decreasing CNT diameter with an exception of the CNT(9,9).

## 1 Introduction

The fast thermal dissipation in graphene-based structures provides a new solution to increase the heat transfer in low conductivity materials. For example, in heat storage systems, solar energy or waste heat can compactly be stored in phase change materials (PCM) in analogy to a charged battery. However, in the discharge mode, the low heat conduction in the PCMs results in a low output power[1], thus limiting its potential applications. One way to solve the problem is by mixing in carbon nanostructures. Recent studies show a manyfold increase in thermal conductivity of PCMs by adding in a mere 5% carbon nanostructures[2–5]. Additional researches on composite materials with carbon structures show the phase equilibrium can be altered in favor of heat storage applications[6,7]. It seems the specific improvement on heat transfer depends not only on the PCM itself, but also on the size, shape, or even the oxidation of the graphene-based structures[8,9]. To further replicate the preliminary successes, more in depth understandings towards the nano-scale carbon-PCM interaction and heat transfer is therefore indispensable.

A viable way to link the nano-scale thermal transport properties to the overall heat conductivity of the complex material is through effective medium approximations. A key parameter used in these approximations is the contact resistance, or Kapitza resistance, $R_K$ [10,11]. In literature referring to carbon nanotubes (CNTs) embedded in various materials, this $R_K$ value varies from 0.76 to 20 $\times 10^{-8}$ Km$^2$/W depending on the matrix material and experimental technique[11–13]. The newly developed PCMs of our interest are sugar alcohols (SA), a category of sugar derived materials with multiple hydroxyl groups. Our aim is to get insight on the nano-scale thermal transport in order to design efficient carbon-PCM composites based on a specific PCM. For such a purpose, it is hard to conclude which $R_K$ value to use in the lack of further carbon-SA system information. To start with, we initiate our research based on carbon-water systems instead. Water is also a high-performance PCM and its phase equilibria and nanoscale heat transfer kinetics are well studied both theoretically and experimentally. The fact that water molecules also possess hydroxyl groups and can form a hydrogen bond network, helps to set up a good basis for and provide insights into our future carbon-SA researches.

Apart from various experimental efforts, many theoretical works have been carried out for both carbon-PCM systems[9,14–17] and carbon-water systems[11,18]. From these works, molecule modeling turned to be a very proficient tool in studying nano-scale thermal transport problems. Using molecular simulation techniques, the heat transfer can be directly monitored and the property calculations are straightforward. It is also advantageous to study the phonon transport, a process potentially important in such nano-structured systems[19–21]. In the work of Hu *et al.*[22], the concept of phonon temperature is used to analyze the internal phonon mode equilibration within graphene layers. This phonon equilibration effect may also influence the carbon-water system.

In this study, we choose molecular dynamics simulations to tackle the cross-plane carbon-water heat transfer problem. The study starts with a 1-D heat transfer problem (graphene-water)

[a] *Address, Technische Universiteit Eindhoven, De Rondom 70, 5612 AP, Eindhoven, the Netherlands. Tel: +31 40 247 3172; E-mail: h.zhang@tue.nl*

† Electronic Supplementary Information (ESI) available: [details of any supplementary information available should be included here]. See DOI: 10.1039/b000000x/

and is then extended to 2-D heat transfer problems (carbon nanotube-water to investigate the geometry effect on the carbon-water heat transfer. In addition to other theoretical works based on various carbon-water interactions, this work is mainly based on a recently developed force field by Pascal *et al.*[23] for its good prediction on mechanical and thermal properties of graphene. We first introduce the molecular simulation method and models in section 2. Then the 1-D graphene-water heat transfer problem is studied in section 3. Using the preferred force field, we extend our study to a variety of single-layer carbon nanotubes (CNT) focusing on the cross plane heat transfer to demonstrate the size effects in section 4. In section 5, we will further discuss on how our results can be applied to determine the overall heat transfer kinetics of complex materials.

## 2 Methodology

### 2.1 Molecular dynamics simulation

In this study, we use molecular dynamics (MD) simulations as the toolbox for quantifying the nanoscale heat transfer phenomena. In MD simulations, the atoms are modeled as point masses which interact with each other according to a set of conservative potentials, called force fields. The system follows Newton's equations of motion. In our non-equilibrium simulations, the temperature coupling is achieved using Nosé-Hoover dynamics[24]. The equation of motion in Nosé Hoover dynamics has an additional term compared with the Newtonian dynamics which is expressed as

$$\frac{\mathrm{d}^2\mathbf{r}_i}{\mathrm{dt}^2} = \frac{\mathbf{F}_i}{m_i} - \frac{p_\xi}{m_\xi}\frac{\mathrm{d}\mathbf{r}_\mathrm{i}}{\mathrm{d}t}, \tag{1}$$

where $m$ is atom mass, $\mathbf{F}_i$ is the resultant force obtained using $\mathbf{r}_i = -\partial E_\mathrm{p}/\partial \mathbf{r}_i$, $\xi$ is a fully dynamics quantity with its own mass $m_\xi$ and momentum defined as $p_\xi = m_\xi \mathrm{d}\xi/\mathrm{d}t$. Esposito and Monnai[24] has shown that systems driven by Nosé-Hoover dynamics allow for a consistent nonequilibrium thermodynamics description. This allows us to calculate the energy flow into a system from the Nosé-Hoover reservoir as

$$Q = \frac{p_\xi^2}{2m_\xi} + 3Nk_\mathrm{B}T\xi, \tag{2}$$

using $\xi$ and $p_\xi$ outputted from the simulation trajectory as extended coordinates.

In the simulations, it is more intuitive to use the period $\tau_T$ of the oscillations of kinetic energy between the system and the reservoir instead of $m_\xi$. The period $\tau_T$ is related to $m_\xi$ via[25]

$$m_\xi = 3Nk_\mathrm{B}\frac{\tau_T^2 T_0}{4\pi^2}, \tag{3}$$

where $T_0$ is the target temperature, $3N$ is the total number of degrees of freedom coupled to the bath. In equilibration simulations, Berendsen thermostat and barostat are used. The $\tau_T$ and $\tau_p$ therein represent the time constant of decay in temperature or pressure in the first order linear system[26].

### 2.2 Intra-carbon and carbon-water interactions

There are many available force fields for graphene-based structures. In this work, we use a QMFF-CX-LJ12-6 (qmcxlj) force field for intra-graphene and intra-carbon nanotube(CNT) interactions[27]. This recently developed force field is claimed to correctly reproduce both thermal and mechanical properties of graphite. On the other hand, this force field is developed towards a dedicated system of pure graphite and not specifically optimized for carbon-water systems. Therefore we choose another two general purposed force fields for comparison: CHARMM (charmm)[28] and generalized AMBER (gaff)[29]. The water model used in this work is the TIP4P-2005 four point model[30]. The model reproduces a good phase diagram of water and is used in various solid-liquid phase change studies[31–33]. We consider this an important aspect since the carbon structures are proposed to function in solid-liquid phase change materials as mentioned in the introduction. The non-bonded interactions between water and carbon follows the LJ12-6 form with Wu and Aluru's parameters[34] specifically designed for water-graphene/CNT simulations.

### 2.3 Simulation setups

There are three different simulation setups in this work, as illustrated in Figure 1. (a) The graphene-water out-of-plane heat transfer simulations use single-layer graphene as heat source at $T_\mathrm{C} = 700$ K and its surrounding water as heat sink at $T_\mathrm{w} = 300$ K. This temperature setting helps to minimize fitting errors in the thermal relaxation simulations while keeping a relatively low carbon temperature. (b) The graphene-water cross-plane simulation uses two graphene layers to separate the water molecules into two compartments. The heat source is the water in one compartment at $T_\mathrm{w1} = 320$ K and the sink is the water in the other compartment at $T_\mathrm{w2} = 280$ K. The first two setups would help to investigate the same problem from tow perspectives: whether to consider graphene as a heat dissipating source or as a thermal transport medium. (c) Similar to the second setup, the periodic CNT separate the water molecules from inside to the outside. The inner molecules are used as heat source at $T_\mathrm{w1}$ and the outer molecules as sink $T_\mathrm{w2}$.

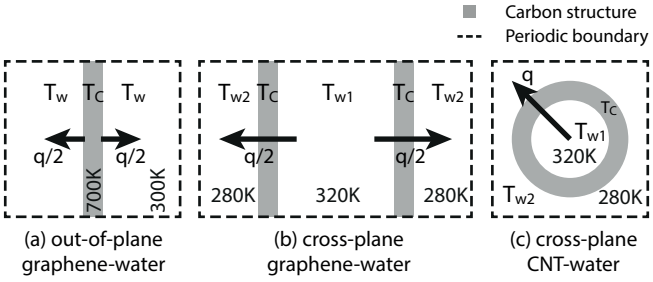


**Fig. 1** Graphical illustration of the simulation setups used in this work. The graphene layers are roughly of sizes 8 nm × 8 nm and the CNTs are about 5 nm or 12 nm long.

In common, all initial configurations are generated using iterative energy minimization and MD equilibration simulations. The equilibration simulations for each simulation are at least 1 ns long and are believed to have reached equilibrium. The detailed

preparation for each setup will be introduced in later sections.

In all simulations, periodic boundary conditions are applied. The time step is set to 1 fs. The rigid water molecules are constrained using LINCS algorithm of order 4 and iterations 4. Particle meshed Ewald summation (PME) is applied to long-range electrostatics with Fourier spacing of 0.12 nm. The long-range LJ interaction is gradually switched off from 1.2 nm to 1.4 nm. In the equilibration simulations, Berendsen thermostat (300 K) and barostat (1.0 bar) are applied with time constant $\tau_T = 0.1$ ps and $\tau_p = 0.5$ ps, respectively. In the non-equilibrium simulations for heat transfer calculation, $\tau_T$ is set to 0.5 ps with no pressure coupling. The trajectories and velocities are outputted every 5 ps and the energies are outputted every 0.1 ps for data analysis.

## 3 Heat transfer between graphene and water

### 3.1 Heat transfer from directly heated graphene

For simulation setup (a), the initial configuration contains 11000 water molecules and a single-layer graphene of 2508 carbons. After equilibration at 300 K, the box size is approximately 8.0 × 8.0 × 5.5 (out-of-plane direction) nm$^3$. The end configuration is named 'conf-A'. The graphene is then heated to 700 K using a Berendsen thermostat while its surrounding water is maintained at 300 K. After simulating for 1 ns, the system is considered as in steady state. We name the end configuration as 'conf-B'. Using conf-B as a starting point, we run a 500 ps non-equilibrium simulation with neither temperature coupling nor pressure coupling (NVE ensemble).

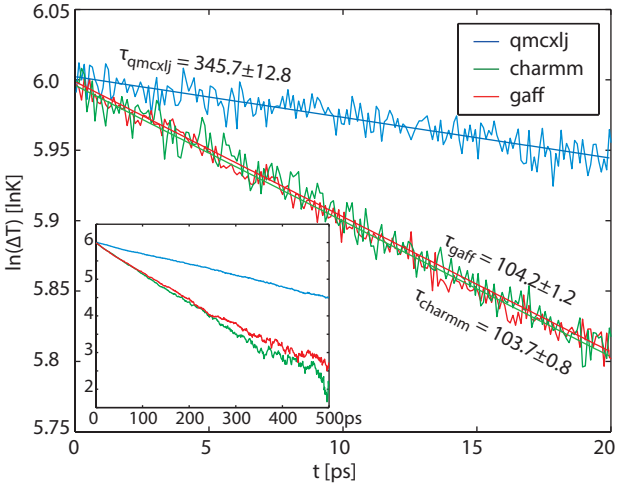


**Fig. 2** The logarithmic temperature differences of different force fields. The curves are not entirely linear because of the temperature dependence. The first 20 ps data are fitted for calculating the time constants $\tau$ at close to $T_C$ = 700K

For each force field, the above procedure is repeated. The temperature of graphene drops as simulations go on. Assuming a constant contact resistance $R_K$ between water and graphene, using the lumped capacitance method, the following equation can be established based on the heat flow rate from graphene to water

$$\frac{dQ}{dt} = -N_C c_C \frac{dT_C}{dt} = N_w c_w \frac{dT_w}{dt} = \frac{2A}{R_K}(T_C - T_w), \quad (4)$$

where $T_C$ and $T_w$ are the temperatures of the graphene layer and the water (Figure 1a), $c_C$ and $c_w$ are the molar heat capacities, $N_C$ and $N_w$ are the number of water molecules and carbon atoms in the system, $A$ is the area of a single contact surface. The equation can be solved in terms of the temperature difference $\Delta T$ between the graphene and water

$$\Delta T(t) = T_C - T_w = \exp\left[-t\frac{2A}{R_K}\left(\frac{1}{N_C c_C} + \frac{1}{N_w c_w}\right)\right] = \exp(-t/\tau), \quad (5)$$

where $\tau$ is the decay time constant which can be fitted as the reciprocal slope of the logarithmic $\Delta T$ curves plotted in figure 2. The linear fits are only applied to the first 20 ps at temperatures close to 700 K. The fitted time constants are listed in table 1. The values in the parenthesis are standard deviations of the fits. Using equation 4, the heat capacity of graphene can also be solved as

$$N_C c_C = -N_w c_w \frac{T_w(t) - T_w(0)}{T_C(t) - T_C(0)}. \quad (6)$$

For convenience, we can rewrite equation 6 as $N_C c_C = \lambda N_w c_w$. Taking $T_C$ and $T_w$ from the simulations and $c_w$ as a known constant, the graphene heat capacity $c_C$ and the ratio $\lambda$ is calculated for each simulation and the results of $c_C$ are listed in table 1. Here, we use the molar heat capacity of TIP4P-2005 water $c_w = 84.71$ J/mol/K reported by Pascal *et al.*[31]. To compare, experimental $c_C^{exp}$ of graphite at is about 8.5 J/mol/K at 300 K[35]. However this does not contradict with the larger simulated values. Both simulated $c_w$ in the reference and simulated $c_C$ in this work are the apparent (classical) molar heat capacities without quantum corrections, since the total conserved energy in the constant energy simulations is calculated as such. This classical $c_C$ is close to the $c_C^{exp}$ at the high temperature limit which is about 25 J/mol/K[35]. In other simulation works, Konatham *et al.*[16] use 23 J/mol/K for contact resistance calculation. Finally, based on equation 5 and the heat capacity ratio $\lambda$, the contact resistance can be obtained as

$$R_K^{DH1} = \frac{2A(1+\lambda)\tau}{N_C c_C}, \quad (7)$$

where the superscript 'DH' abbreviates 'directly heated'. Values of $R_K^{DH1}$ are listed in table 1.

Although the above thermal relaxation method has been used in many studies as an ordinary way to characterize $R_K$ [11,16], the temperature dropping in graphene may have influences on the $R_K$ value. To characterize $R_K$ at a constant temperature, we propose to use the source-sink algorithm with Nosé-Hoover thermostat. The total amount of heat $Q$ transferred from graphene to water can be easily monitored and calculated using equation 2. For comparison and validation purposes, we choose conf-B as a starting point and run a 500 ps non-equilibrium simulation with Nosé-Hoover thermostat and no pressure coupling. After the sim-

ulations, the contact resistances are calculated using

$$R_{\mathrm{K}}^{\mathrm{DH2}} = 1/U_{\mathrm{K}}^{\mathrm{DH2}} = 2A\Delta T/q, \tag{8}$$

where $U_{\mathrm{K}}^{\mathrm{DH2}}$ is the corresponding heat transfer coefficient, $q$ is the heat transfer rate from carbon to both sides of water fitted as the slope in the $Q$-$t$ curves (Figure S1 in the supplementary materials). The area of the graphene layer $A$ is the same as used in equation 7. The temperature jumps at the boundary $\Delta T$ are fitted using the temperature profiles of water and extrapolated to the outmost position, similar to those defined in section 3.2. The calculated $U_{\mathrm{K}}^{\mathrm{DH2}}$ and $R_{\mathrm{K}}^{\mathrm{DH2}}$ are listed in table 1.

The $R_{\mathrm{K}}$ values from both methods show good agreement in the range of the standard deviations. In ordinary non-equilibrium simulations utilizing Fourier's conduction law, the source and the sink are placed far apart and only the linear temperature profile region is used to calculate the temperature gradient[36]. This is because the Fourier's conduction law applies only to the diffusive transfer regime with a linear temperature profile[37]. Close to the thermostats, at distances below a phonon mean free path, the temperature profiles are no longer linear. It is not clear whether this non-diffusive behavior is influenced or even induced by the thermostats. Similarly, in the case of directly heated graphene, it is not known if the thermostat can influence the temperature jump at the boundary and hence the heat transfer rate. By comparing the resistance values calculated using relaxation method and source-sink method, we are convinced the thermostats directly in contact have no major impact on the heat transfer rate. Therefore, the simulations done after this subsection use only the source-sink algorithm, for its advantage in maintaining constant temperature differences.

It is observed from table 1 that the qmcxlj force field results in a higher contact resistance compared with the other two. The equivalent Kapitza radius $r_{\mathrm{K}} = R_{\mathrm{K}}k_{\mathrm{w}}$, representing the distance from the interface where the temperature drops the same amount as it drops at the interface under the same heat flux, is about 287 nm in this case, given the experimental heat conductivity of water $k_{\mathrm{w}}^{\mathrm{exp}} = 0.63$ W/m/K. This large $r_{\mathrm{K}}$ value could cancel much of the advantage of adding carbon structures of sub-micron sizes. As comparison, other literature studies reported a range from $0.76 \times 16^{-8}$ to $20.0 \times 16^{-8}$ m$^2$/K/W resistances values using various theoretical and experimental techniques[11,13].

### 3.2 Heat transfer across single-layer graphene

Bearing in mind the ballistic heat transfer characteristics of the nano-scale structures, we realize that the heat transfer across the graphene layer may be different[8]. Therefore, to backup and compare the counter-intuitively high resistance values, simulations are carried out using setup b (Figure 1b). To start, conf-A is duplicated in the out-of-plane direction. The two compartments of water and graphene layers are then coupled to 280 K, 320 K, and 300 K, respectively, at 1.0 bar for 1000 ps as equilibration processes. After equilibration, the thermostat for graphene is removed while the thermostats for water are switched to Nosé-Hoover with no pressure coupling for 500 ps.

Using the 500 ps simulation data, a steady state density profile and temperature profile can be established, as illustrated in Figure 3. As a finite temperature effect, the density peaks at the low temperature region $z > 0$ are higher than those on the other side. The qmcxlj gives a higher carbon density peak. This usually means the qmcxlj graphene is more rigid and might be the reason of its large $R_{\mathrm{K}}$. In Figure 3, there is an evident temperature jump $\Delta T$ near the interface. This jump can be quantified using curve fitting tools. In the liquid region, the phonon mean free paths are very short. Therefore the heat transfer within the liquid region can be considered to be diffusive. Because the thermostat on water removes statistically the same amount of energy per molecule, or, approximately the same amount of energy per unit volume, the temperature profile of water along the out-of-plane direction should be quadratic in the diffusive heat transfer regime. Therefore we use quadratic curves to fit $T_{\mathrm{w}}(x)$ and extrapolate $\Delta T$. In fact, the thermal conductivity of water $k_{\mathrm{w}}$ is related to the second derivative of the fitted profile $T_{\mathrm{w}}(x)$ via

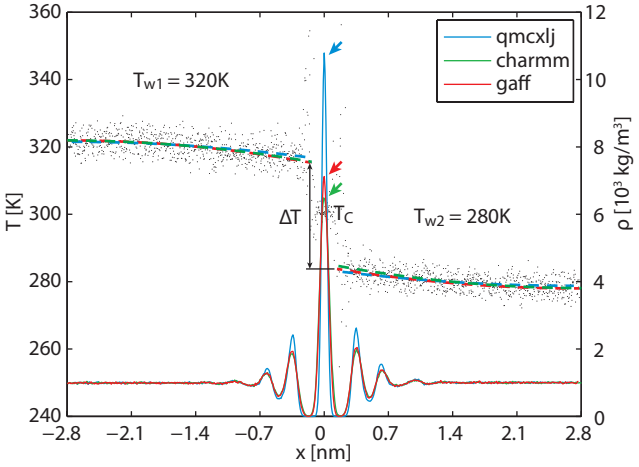


**Fig. 3** The temperature and density profiles in the steady-state cross-plane heat transfer simulations. The gray dashed lines are the temperature profiles with larger variance at near-zero density regions. The colored dashed lines are linearly fitted temperatures weighted by the local number densities.

$$q_{\mathrm{V}} = \frac{q}{2AL_{\mathrm{w}}} = k_{\mathrm{w}}\frac{\mathrm{d}^2T}{\mathrm{d}x^2}, \tag{9}$$

where $q_{\mathrm{V}}$ is the volumetric heat generation rate and $L_{\mathrm{w}}$ is the length of water in one compartment. The calculated $k_{\mathrm{w}}$ values are listed in the last column of table 1. The numbers in the parenthesis are the standard deviations calculated from the fits. The values show good agreement with $k_{\mathrm{w}} = 0.91(1)$ W/m/K of bulk TIP4P-2005 water[38], which acts as a good validation for our fittings. To be noted, the fits are weighted by the number densities of water molecules to minimize the influence of large uncertainties at near-zero density regions.

Using $\xi$ and $p_\xi$ outputted from the simulation and equation 2, the heat flow $Q$ across the graphene layer over time is computed. The heat flow rate $q$ can then be fitted as the slope of the $Q$-$t$ curves (Figure S1 in the supplementary materials). Finally, the cross-plane contact resistance is calculated according to its defi-

**Table 1** Graphene-water contact resistance calculated using graphene as heat source or using graphene as a heat transfer medium

| Force field | $\tau$/(ps) | $c_C$/(J/mol/K) | $R_K^{DH1}$/(m$^2$K/W) | $U_K^{DH2}$/(W/m$^2$/K) | $R_K^{DH2}$/(m$^2$K/W) | $U_K^{CP}$/(W/m$^2$/K) | $R_K^{CP}$/(m$^2$K/W) | $k_w$/(W/m/K) |
|---|---|---|---|---|---|---|---|---|
| qmcxlj | 345(13) | 24.5(10) | $46.9(39)\times10^{-8}$ | $2.197(1)\times10^{6}$ | $45.52(2)\times10^{-8}$ | $95.0(3)\times10^{6}$ | $0.526(2)\times10^{-8}$ | 0.95(6) |
| charmm | 104(1) | 24.4(6) | $13.5(5)\times10^{-8}$ | $7.851(3)\times10^{6}$ | $12.73(1)\times10^{-8}$ | $141.6(5)\times10^{6}$ | $0.353(1)\times10^{-8}$ | 0.90(5) |
| gaff | 104(1) | 24.3(7) | $13.9(6)\times10^{-8}$ | $7.752(3)\times10^{6}$ | $12.90(1)\times10^{-8}$ | $129.1(4)\times10^{6}$ | $0.387(1)\times10^{-8}$ | 0.89(7) |

Note: Values in the parenthesis represent standard deviations of the last digits. Other related calculation data are given in table S1-S3.

nition

$$2R_K^{CP} = 1/U_K^{CP} = 2A\Delta T/q, \quad (10)$$

where the superscript 'CP' abbreviates 'cross-plane'. The left side factor 2 represents the sum of two equal $R_K$ values on both sides of the graphene. The values of $R_{K,CP}$ calculated are listed in table 1 while $\Delta T$, $A$, and $q$ are provided in the supplementary materials (table S3). It is noticeable that $R_K^{CP}$ is much smaller than $R_K^{DH}$ obtained in the previous subsection. This difference will be discussed in section 3.3.

### 3.3 Phonon equilibration within the carbon structure

The order of magnitude difference between $R_K^{DH}$ (at 700 K) and $R_K^{CP}$ (at 300 K) in table 1 is striking. Additional simulations at $T_C = 320$ K show $R_K^{DH}$ equals to 51.4(14), 16.3(2), and 16.5(2) $\times10^{-8}$ m$^2$K/W, for the three force fields respectively (see table S4), resulting in even larger resistance values. The major difference lies between the two simulation setups. The same discrepancy was observed by Hu *et al.*[22]. By applying a thermostat, the energy is equally pumped to all vibration modes. However, only the low frequency phonons participate in the out-of-plane heat transfer[39]. This brings in an additional equilibration process within the carbon structure which acts as an extra resistance. Because the qmcxlj carbon is more rigid, the high frequency phonons are harder to scatter and hence the resistance $R_K$ is higher. In fact, the low frequency heat carrying phonons (below 300 cm$^{-1}$) can transmit through the graphene layer, following a ballistic transfer path[20,21,39,40]. To further prove this, we calculated the phonon density of states (DoS) of graphene in both conf-A and conf-B, by additional 20 ps simulations with no temperature or pressure coupling. The DoS of conf-A ($S_{eq}$) is considered as an equilibrium DoS while the DoS of conf-B ($S_{neq}$) is considered as a non-equilibrium DoS. The phonon temperatures as function of their frequencies can then be expressed as

$$T_{neq}(\nu) = T_{eq}\frac{S_{neq}(\nu)}{S_{eq}(\nu)}, \quad (11)$$

where $\nu$ denotes frequency, and $T_{eq} = 300K$ is the equilibrium temperature. In Figure 4, the low frequency phonons are closer to 300 K in all three cases. This indicates a thermal equilibrium between the low frequency phonons with the surrounding water molecules. The kinetic energy carried by the high frequency phonons have to scatter to the low frequency phonons before transmitted to the surrounding water.

Indeed, the two systems illustrated in Figure 1a and 1b are not the same heat transfer problem. In fact, both $R_K$ values represent reality, with the one from thermal relaxation in analogy to a laser flash experiment while the cross-plane value representing a traditional axial flow method. In carbon structure enhanced composite materials, the liquid matrix material is the major heat carrier. The heat transferred to either graphene or CNT needs to be transferred back to the matrix material. This is in contrast with systems using carbon micro/nano fins for chip cooling. Therefore we consider the cross-plane resistance as a more reasonable choice to characterize the contact resistance.

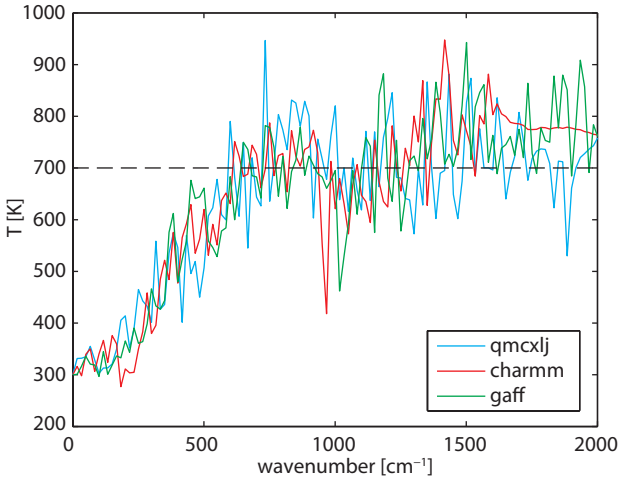


**Fig. 4** Non-equilibrium phonon temperature of graphene at various frequencies. The mean graphene temperature is at 700 K while its surrounding water is at 300 K.

## 4 Geometry Effects on Cross-plane Heat Transfer

Apart from graphene nano-platelets, CNTs are also common additives for heat conduction enhancement. Prior research has shown dramatic geometry effects on another transport property —diffusivity[41]. When the confinement size of CNT is comparable to the water molecules' diameter, the water inside may form special structures and behave differently from their bulk state[42]. This geometry effect may influence the water-carbon heat transfer as well. We hence consider it necessary to check if the CNTs have the same contact resistances as the planer graphenes.

CNTs with 10 different diameters are modeled, all in armchair configuration. The CNT(30,30) to CNT(10,10) are 5 nm in length, while the CNT(9,9) to CNT(6,6) are 12 nm in length. These CNTs are solvated in either 7500 or 12000 water molecules at 300 K and equilibrated for 1.5-3.0 ns, depending on when the number of water molecules inside the tubes become steady. Then the equilibrium structures along with the water molecules inside are extracted from the end configurations and rotated to align the z-axis of the simulation boxes. These structures are then applied with periodic boundary conditions to form periodic tubes. The top view of the thinnest tubes along with the solvent molecules

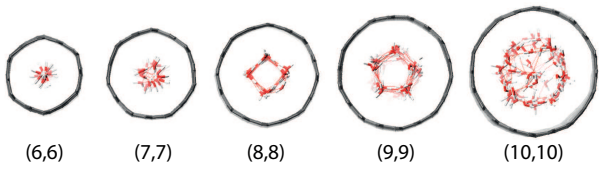


**Fig. 5** The top view of the thinnest CNTs with water inside after equilibration.

enclosed are illustrated in figure 5. These periodic tubes are then solvated into 4500-9000 water molecules and equilibrated for another 1 ns. The above steps are similar to those used by Pascal *et al*.[42]. After this preliminary equilibration, the inside water, the CNTs, and the outside water are coupled to 320 K, 300 K, and 280 K, respectively, for an additional 500 ps equilibration, at pressures of 1.0 bar. This is to prepare the initial configuration for the heat transfer simulation. Lastly, the temperature coupling is switched to Nosé-Hoover for both water inside and outside the CNT. For CNT itself, the temperature coupling is switched off. The pressure coupling for the system is also switched off. Simulations of 500 ps long are used to calculate the cross-plane heat transfer.

### 4.1 Equilibrium structures and density profiles

The equilibrium structures strongly depend on the CNT diameter. In CNT(6,6) and CNT(7,7), the narrow tube diameters only allow water molecules to align on the central axis. In CNT(8,8) and CNT(9,9), the diameters are larger allowing water molecules to form a "ring" structure, resulting in a larger in-tube water number density. The number of confined water molecules per unit length of CNT $N$ is given in table 2. Also given in the table are the tube diameters $d$ and the effective density $\rho_{\text{eff}}$ of the confined water. This effective density is calculated based on the effective diameter defined as $d_{\text{eff}} = d - \sqrt[6]{2}\sigma_{\text{CO}}$, where $\sigma_{\text{CO}} = 0.34352$ nm is the radius term between carbon and oxygen atoms in the Lennard-Jones potential. To be noted, the effective density of water in CNT(8,8) is higher than the bulk value of 997 kg/m$^3$.

**Table 2** Number of confined water molecules and cross-plane heat transfer coefficient of various sized CNTs

| CNT | $d$/(nm) | $N/l$/(nm$^{-1}$) | $\rho_{\text{eff}}$/(kg/m$^{-3}$) | $U^{\text{CP}}$/(W/m$^2$/K) |
|---|---|---|---|---|
| graphene | $+\infty$ | $+\infty$ | 997* | 95.0(3) $\times 10^6$ |
| (30,30) | 4.029(5) | 349.0(25) | 1001(8) | 91.0(10)$\times 10^6$ |
| (20,20) | 2.693(3) | 139.3(13) | 997(10) | 84.9(7) $\times 10^6$ |
| (17,17) | 2.288(1) | 93.7(13) | 987(14) | 79.2(9) $\times 10^6$ |
| (14,14) | 1.884(0) | 58.0(10) | 983(16) | 71.3(10)$\times 10^6$ |
| (12,12) | 1.615(1) | 38.6(7) | 972(18) | 66.2(13)$\times 10^6$ |
| (10,10) | 1.347(0) | 23.5(4) | 966(18) | 54.7(14)$\times 10^6$ |
| (9,9) | 1.210(0) | 17.4(2) | 977(9) | 9.4(11) $\times 10^6$ |
| (8,8) | 1.076(0) | 13.8(1) | 1101(12) | 26.0(11)$\times 10^6$ |
| (7,7) | 0.941(0) | 4.8(2) | 588(20) | 10.5(4) $\times 10^6$ |
| (6,6) | 0.806(1) | 3.6(0) | 785(11) | 8.0(7) $\times 10^6$ |

*Water bulk density at 300 K

The density profile in the radial direction is plotted in Figure 6. The density peaks roughly sit at the same positions in all cases. In general, smaller tubes give rise to more evident density peaks. In particular, CNT(6,6) has a strong primary peak and CNT(10,10) has a strong secondary peak. The steady state temperature profiles in the radial direction resemble those plotted in Figure 3, with quadratic temperature profiles on the left (inner) side of the CNT layers and temperature jumps on both sides of the CNTs.

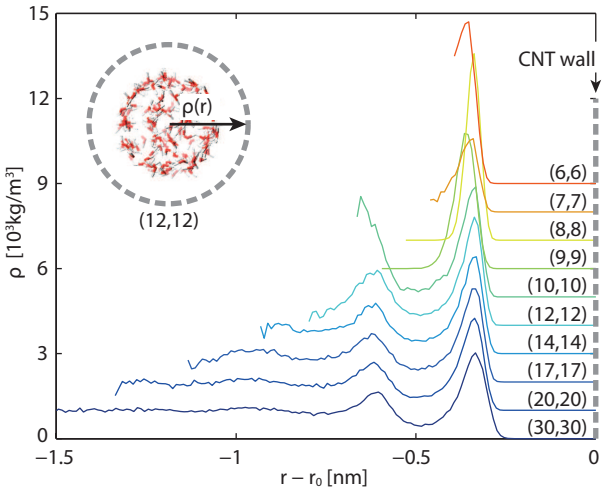


**Fig. 6** Density profiles of in-tube water in the radial direction. The densities are shifted 1000 kg/m$^3$ each upward. Horizontal axis labels the radial position relative to the CNT wall.

### 4.2 Heat transfer coefficient

The cross plane water-water heat transfer coefficients $U^{CP}$ are calculated in a similar way as described in section 3.2 and are plotted in figure 7 and listed in table 2. As the diameter decreases, the heat transfer coefficient also decreases, but not monotonically. We see a dramatic decrease in the CNT(9,9) case, and a moderate increase in CNT(8,8).

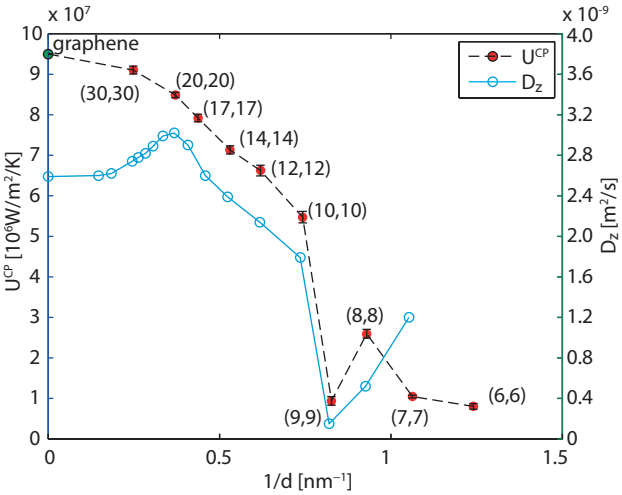


**Fig. 7** Heat transfer coefficients across the CNTs and axial diffusion coefficient[41] versus reciprocal diameter. In the limit of infinite diameter, the result of graphene is marked.

The water in CNT(9,9) in many studies is believed to be ice-like, which may help explain the low heat transfer coefficient. In literature, the ice-like structure is related to the stronger hydrogen bonds[43] and its enthalpy stabled structure[42] which leads to a very low spatial diffusivity[41,43]. The ice-like structure inside the CNT(9,9) results in a phonon mode mismatch to the liquid water outside and hampers the heat transfer[22], in analogy to the graphene-water heat transfer described in section 3.1. To get more details on the fundamental differences between water confined in CNT(9,9) and CNT(10,10), we further calculated the phonon density of state of water in both cases. The results are plotted in figure 8 with reference to bulk liquid water and solid ice-Ih. The water in CNT(10,10) is indeed liquid-like. The flatter curve indicates more phonon scattering and the non-zero spectral density at zero frequency shows the molecules are diffusive[44]. On the other hand, the water confined in CNT(9,9) is almost non-diffusive. The phonons are less scattered at lower frequencies. At wavenumber above 170 $cm^{-1}$, there are some red shifts of the spectral peaks compared to the bulk solid curve and the peak heights are lower. Therefore, although the water is solid-like, it should be distinguished from the solid ice Ih state. In the case of CNT(8,8), the heat transfer coefficient is higher than both its neighbours. Compared with CNT(9,9), the single-file diffusion[41] may allow the water inside to couple with some low frequency phonon modes for a more efficient heat transfer. Here we have noticed an interesting correlation between $U^{CP}$ and the axial diffusion coefficient of confined water[41] from CNT(20,20) to CNT(8,8) according to Figure 7. However, the correlation breaks in the case of CNT(7,7) and the heat transfer rate seems to drop alongside the effective density (47% vs. 60% drop in table 2). This correlation is not surprising considering the major component of heat transfer, the kinetic energy transfer, scales with the number density of interacting molecules[45].

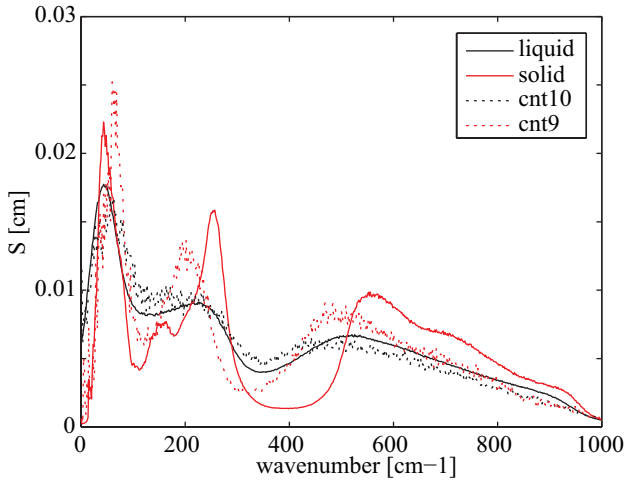


**Fig. 8** Phonon density of state of water confined in CNT(10,10) and CNT(9,9) with reference to bulk liquid water and overheated ice-Ih, both at 300 K.

## 5 Discussion

The results presented in section 3 shows that the heat transfer from graphene to water is not simply dependent on the overall temperature of the graphene, but also depends on the different mode contributions to the temperature —the Fourier transformed kinetic energy in the form of phonon temperatures. This is in line with the ballistic heat transfer mechanisms often observed in nano-scale systems[8]. In the use of graphene or CNTs as additives for heat conduction enhancement, the heat first flows into the carbon structure and takes the advantage of the fast thermal dissipation of the carbon before the heat is conducted out. In this process, the phonons as heat carriers travel through the carbon structure. Although the overall contact resistance between carbon and water is quite high, the phonon transmission coefficient for low frequency phonons is high, allowing fast thermal equilibration of low frequency phonons to the environment[39]. According to Saaskilahti *et al*., the low frequency phonons are also the main heat carriers within the CNTs and have much higher spectral thermal conductivity[46]. In this way, the graphene or CNT can still work as a good additive for the PCMs. The high overall carbon-water resistance $R_K^{DH}$ underestimates the heat carrying capability of the low frequency phonons while the cross-plane resistance $R_K^{CP}$ characterizes the resistance for low frequency heat carrying phonons. In fact, direct simulations of mixed graphene platelets and PCM would not be observed with any substantial gain in conductivity if to use the Kapitza radius $r_K$ at around 100 nm (section 3.1). This is in contrary to the work of Huang *et al*. where 30% gain is observed using graphene nano-platelets as additives[47]. Therefore, we recommend to use the cross-plane $R_K^{CP}$ as the resistance for estimating the effective conductivity of

the carbon-PCM composites, when an effective medium approach is applied[11].

Based on the results of section 4, the nano-scale confinement has obviously altered the properties of water inside. Although the heat transfer trends lower at smaller sized tubes, the trend is not monotonic (Figure 7). At diameters less than 1.2 nm, the properties of water confined become case-specific. To be noted, in these narrow tube cases, the heat transfer coefficient has decreased one order of magnitude. If converted to the Kapitza resistance using $R_K = 1/(2U)$, the values corresponds to an increase from the graphene case of 0.5 $\times 10^{-8}$ m$^2$/K/W to the CNT(6,6) case of 6.2 $\times 10^{-8}$ m$^2$/K/W. In this argument, the smaller sized tubes may be unfavorable to be used as additives for heat transfer enhancement if their lengths are the same.

## Conclusions

Using molecular dynamics simulation method and advanced data analyzing techniques, the cross-plane heat transfer of single-layer carbon structures submerged in liquid water is studied in depth. In this study, we found the heat transfer kinetics across graphene from water to water is much faster than the heat transfer from graphene to their surrounding water molecules. The dramatic difference lies within the non-diffusive nature of heat transfer in nano-scale systems. Both cross-plane and out-of-plane systems are studied quantitatively and characterized using Kapitza resistance. We showed the cross-plane resistance $R_K^{CP}$ represents better the resistance for low frequency phonons, which are the major heat carriers. Therefore the $R_K^{CP}$ values are more favorable to be used in effective medium approaches for effective conductivity calculation of composites. The research is further extended to CNT-water systems to include the size effect of wrapped graphene layers. We found that the heat transfer coefficients decrease with decreasing diameter, but not monotonically. The very low heat transfer coefficient across CNT(9,9) is found to be related to the water confined forming an ice-like structure. The results obtained in this research provided deeper understanding on the nano-scale heat transfer of carbon structures submerged in water and used as conductivity enhancement additives, and provided valuable data for carbon-PCM composite material designs.

## Acknowledgements

The research leading to these results has received funding from the European Community's Seventh Framework Programme (FP7/2007-2013) under grant agreement 296006.

## References

1 L. Fan and J. Khodadadi, *Renewable and Sustainable Energy Reviews*, 2011, **15**, 24–46.
2 F. Yavari, H. R. Fard, K. Pashayi, M. A. Rafiee, A. Zamiri, Z. Yu, R. Ozisik, T. Borca-Tasciuc and N. Koratkar, *The Journal of Physical Chemistry C*, 2011, **115**, 8753–8758.
3 W. Yu, H. Xie, X. Wang and X. Wang, *Physics Letters A*, 2011, **375**, 1323–1328.
4 M. Li, *Applied energy*, 2013, **106**, 25–30.
5 L.-W. Fan, X. Fang, X. Wang, Y. Zeng, Y.-Q. Xiao, Z.-T. Yu, X. Xu, Y.-C. Hu and K.-F. Cen, *Applied Energy*, 2013, **110**, 163–172.
6 W. Alshaer, E. P. del Barrio, M. Rady, O. Abdellatif and S. Nada, *Int. J. Heat Mass Transf. Theory Appl. IREHEAT*, 2013, **1**, 297–307.
7 J.-N. Shi, M.-D. Ger, Y.-M. Liu, Y.-C. Fan, N.-T. Wen, C.-K. Lin and N.-W. Pu, *Carbon*, 2013, **51**, 365–372.
8 A. M. Marconnet, M. A. Panzer and K. E. Goodson, *Reviews of Modern Physics*, 2013, **85**, 1295.
9 Y.-R. Huang, P.-H. Chuang and C.-L. Chen, *International Journal of Heat and Mass Transfer*, 2015, **91**, 45–51.
10 E. T. Swartz and R. O. Pohl, *Reviews of modern physics*, 1989, **61**, 605.
11 V. Unnikrishnan, D. Banerjee and J. Reddy, *International Journal of Thermal Sciences*, 2008, **47**, 1602–1609.
12 S. T. Huxtable, D. G. Cahill, S. Shenogin, L. Xue, R. Ozisik, P. Barone, M. Usrey, M. S. Strano, G. Siddons, M. Shim *et al.*, *Nature materials*, 2003, **2**, 731–734.
13 A. A. Balandin, SPIE NanoScience+ Engineering, 2011, pp. 810107–810107.
14 N. Singh and D. Banerjee, 2010 14th International Heat Transfer Conference, 2010, pp. 427–431.
15 H. Babaei, P. Keblinski and J. Khodadadi, *International Journal of heat and mass transfer*, 2013, **58**, 209–216.
16 D. Konatham, D. Papavassiliou and A. Striolo, *Chemical Physics Letters*, 2012, **527**, 47–50.
17 N. Singh, V. Unnikrishnan, D. Banerjee and J. Reddy, *International Journal for Computational Methods in Engineering Science and Mechanics*, 2011, **12**, 254–260.
18 S. Maruyama, Y. Igarashi, Y. Taniguchi and Y. Shibuta, Proceedings of the First International Symposium on Micro and Nano Technology, 2004.
19 A. A. Balandin and D. L. Nika, *Materials Today*, 2012, **15**, 266–275.
20 L. Chen, Z. Huang and S. Kumar, *Applied Physics Letters*, 2013, **103**, 123110.
21 M. Shen and P. Keblinski, *Journal of Applied Physics*, 2014, **115**, 144310.
22 L. Hu, T. Desai and P. Keblinski, *Physical Review B*, 2011, **83**, 195423.
23 T. A. Pascal, N. Karasawa and W. A. Goddard III, *The Journal of chemical physics*, 2010, **133**, 134114.
24 M. Esposito and T. Monnai, *The Journal of Physical Chemistry B*, 2010, **115**, 5144–5147.
25 B. Hess, C. Kutzner, D. van der Spoel and E. Lindahl, *J. Chem. Theory Comput.*, 2008, **4**, 435–447.
26 H. J. Berendsen, J. P. M. Postma, W. F. van Gunsteren, A. DiNola and J. Haak, *The Journal of chemical physics*, 1984, **81**, 3684.
27 T. A. Pascal, N. Karasawa and W. A. Goddard III, *The Journal of chemical physics*, 2010, **133**, 134114.
28 A. D. MacKerell, D. Bashford, Bellott, R. L. Dunbrack, J. D. Evanseck, M. J. Field, S. Fischer, J. Gao, H. Guo, S. Ha, D. Joseph-McCarthy, L. Kuchnir, K. Kuczera, F. T. K. Lau,

C. Mattos, S. Michnick, T. Ngo, D. T. Nguyen, B. Prodhom, W. E. Reiher, B. Roux, M. Schlenkrich, J. C. Smith, R. Stote, J. Straub, M. Watanabe, J. WiÃşrkiewicz-Kuczera, D. Yin and M. Karplus, *The Journal of Physical Chemistry B*, 1998, **102**, 3586–3616.

29 J. Wang, R. M. Wolf, J. W. Caldwell, P. A. Kollman and D. A. Case, *Journal of Computational Chemistry*, 2004, **25**, 1157–1174.

30 J. L. Abascal and C. Vega, *The Journal of chemical physics*, 2005, **123**, 234505.

31 T. A. Pascal, D. Schärf, Y. Jung and T. D. Kühne, *The Journal of chemical physics*, 2012, **137**, 244507.

32 E. Sanz, C. Vega, J. R. Espinosa, R. Caballero-Bernal, J. L. F. Abascal and C. Valeriani, *Journal of the American Chemical Society*, 2013, **135**, 15008–15017.

33 J. Benet, L. G. MacDowell and E. Sanz, *Physical Chemistry Chemical Physics*, 2014, **16**, 22159–22166.

34 Y. Wu and N. Aluru, *The Journal of Physical Chemistry B*, 2013, **117**, 8802–8813.

35 E. Pop, V. Varshney and A. K. Roy, *MRS Bulletin*, 2012, **37**, 1273–1281.

36 J. Shiomi, *Annual Review of Heat Transfer*, 2014, **17**, 177–203.

37 M. Wang, N. Yang and Z.-Y. Guo, *Journal of Applied Physics*, 2011, **110**, 064310.

38 Y. Mao and Y. Zhang, *Chemical Physics Letters*, 2012, **542**, 37–41.

39 M. Shen, P. K. Schelling and P. Keblinski, *Physical Review B*, 2013, **88**, 045444.

40 P. Keblinski, S. Phillpot, S. Choi and J. Eastman, *International journal of heat and mass transfer*, 2002, **45**, 855–863.

41 A. Barati Farimani and N. Aluru, *The Journal of Physical Chemistry B*, 2011, **115**, 12145–12149.

42 T. A. Pascal, W. A. Goddard and Y. Jung, *Proceedings of the National Academy of Sciences*, 2011, **108**, 11794–11798.

43 L. B. Da Silva, *Journal of Nanostructure in Chemistry*, 2014, **4**, 1–5.

44 T. A. Pascal, S.-T. Lin and W. A. Goddard III, *Physical Chemistry Chemical Physics*, 2011, **13**, 169–181.

45 G. Bird, *Molecular Gas Dynamics and the Direct Simulation of Gas Flows*, Clarendon Press, 1994.

46 K. Sääskilahti, J. Oksanen, S. Volz and J. Tulkki, *Physical Review B*, 2015, **91**, 115426.

47 X. Huang, W. Xia and R. Zou, *Journal of Materials Chemistry A*, 2014, **2**, 19963–19968.

## Supplementary materials

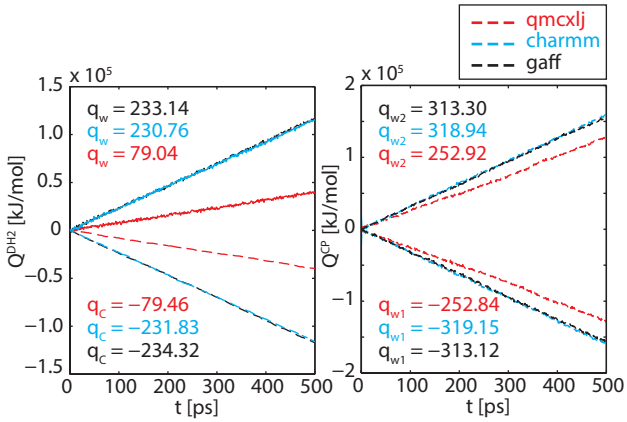


Figure S1. The heat flow over time in the calculation of $R_K^{DH2}$ and $R_K^{CP}$. The fitted slopes of the heat sources and sinks are given as $q$.

Table S1. $A$ and $\lambda$ used in the calculation of $R_K^{DH1}$

| Force field | $A$ /(nm$^2$) | $\lambda$ |
|---|---|---|
| qmcxlj | 64.856 | 6.61(27)% |
| charmm | 61.906 | 6.56(16)% |
| gaff | 63.357 | 6.53(19)% |

Data in parenthesis marks the standard deviation (std) of the last digits

Table S2. $q$, $A$, and $\Delta T$ used in the calculation of $R_K^{DH2}$

| Force field | $q$ /(kJ/mol/ps) | $A$ /(nm$^2$) | $\Delta T$ /K |
|---|---|---|---|
| qmcxlj | 79.25(2) | 64.856 | 397.1(1) |
| charmm | 231.29(2) | 61.906 | 395.2(1) |
| gaff | 233.73(2) | 63.357 | 395.1(1) |

Data in parenthesis marks the std of the last digits. For $\Delta T$, the std is calculated from the uncertainties of the extrapolation as the true mean response. This is to be distinguished from the prediction bound.

Table S3. $q$, $A$, and $\Delta T$ used in the calculation of $R_K^{CP}$

| Force field | $q$ /(kJ/mol/ps) | $A$ /(nm$^2$) | $\Delta T$ /K |
|---|---|---|---|
| qmcxlj | 252.9(1) | 64.839 | 34.08(9) |
| charmm | 319.0(1) | 61.992 | 30.18(10) |
| gaff | 313.2(1) | 63.447 | 31.75(9) |

Data in parenthesis marks the std of the last digits. For $\Delta T$, the std is calculated from the uncertainties of the extrapolation as the true mean response. This is to be distinguished from the prediction bound.

Table S4. Calculation of $R_K^{DH2}$ at 320K

| Force field | $q$ /(kJ/mol/ps) | $A$ /(nm$^2$) | $\Delta T$ /K | $R_K^{DH2}$/(m$^2$K/W) |
|---|---|---|---|---|
| qmcxlj | 2.98(8) | 64.840 | 19.63(4) | 51.4(14) $\times 10^{-8}$ |
| charmm | 9.15(9) | 61.992 | 20.14(4) | 16.3(2) $\times 10^{-8}$ |
| gaff | 8.89(1) | 63.444 | 19.91(4) | 16.5(2) $\times 10^{-8}$ |

The coalitions are based on $T_C$ = 320 K and $T_w$ = 300 K. Because of the much less heat transfer rate, each results are averaged over 400 configurations sampled in a 2 ns simulation.